

COMPUTATIONAL INVESTIGATION OF MICRO HOVERING ROTOR AERODYNAMICS

Vinod K. Lakshminarayan*,
James D. Baeder†

Alfred Gessow Rotorcraft Center,
Department of Aerospace Engineering,
University of Maryland, College Park, MD 20742.

Abstract

In this work, a compressible Reynolds Averaged Navier Stokes (RANS) code is used to investigate low Reynolds number and low Mach flows, which are typical of Micro Air Vehicles (MAV). The main objective of this work is to assess the predictive capability and to identify the deficiencies of the computational methodology. The code is validated with experiments for 2D airfoil flows in order to assess the lift and drag predictions. 3D finite wing validations are performed to ascertain the capability of the methodology to predict tip vortex evolution. This is then followed by extensive validation studies on micro hovering rotors. A recurring theme in all these calculations is that inviscid phenomena like lift/thrust and tip vortex structure/induced velocities are modeled well, while drag/power predictions show considerable deviation from experimental data with the exception of Micro-rotor 2. It appears that the discrepancy arises mainly because of the difference between modeled and actual geometry in the leading edge and trailing edge regions. Tip vortex parameters are well captured except for the core size is computed to be slightly larger than the experimental measurements and more vorticity is entrained into the tip vortex than is measured.

Nomenclature

c	Chord length of the airfoil
R	Radius of the rotor
M_∞	Free-stream Mach number
M_{tip}	Tip Mach number
V_{tip}	Tip Speed
Re	Reynolds Number
α	Angle of Attack
ψ	Wake age (degrees)
θ_o	Collective pitch (degrees)
C_T	Thrust Coefficient = Thrust/ $(\rho\pi R^2 V_{tip}^2)$
C_P	Power Coefficient = Power/ $(\rho\pi R^2 V_{tip}^3)$
FM	Figure of Merit = Ideal Power/Actual Power (Ideal Power = $\frac{C_T^{3/2}}{\sqrt{2}}$)
Γ_b	Bound circulation on the blade (normalized by speed of sound and blade chord)
Γ_v	Vortex circulation (normalized by speed of sound and blade chord)

ω	Vorticity vector (normalized by speed of sound and blade chord)
q	Non-dimensionalized Invariant of the velocity gradient tensor $\frac{\partial u_i}{\partial x_j} \frac{\partial u_j}{\partial x_i}$ (normalized by speed of sound and blade chord)
r_c	Core radius (normalized by chord)

Introduction

With the growing desire for efficient rotary wing MAV which typically operate between $Re = 10^3 - 10^5$, accurate predictions of low Mach, viscous dominated flows are in increasing demand. Because of the difficulties involved in experimentally studying MAV and the breakdown of analytical correlations for drag and boundary layer behavior for this Reynolds number range, accurate computational results are of critical importance to MAV research. The goal of this work is to extend the applicabil-

* Graduate Research Assistant, vinodkl@umd.edu

† Associate Professor, baeder@eng.umd.edu

ity of a compressible Reynolds Averaged Navier-Stokes (RANS) solver for analysis of the flow physics to the low Mach and Reynolds number regime; a condition that has not yet received a considerable amount of computational attention. In a more general sense, extending the confidence in predictions in this problem ultimately leads towards a more detailed characterization of the flow physics over the entire Mach and Reynolds number spectrum using a single solver.

Background

Low Reynolds number flow is well understood from a theoretical viscous flow perspective, however computational validation of experimental data has barely been conducted in the Reynolds number range of 20,000 to 100,000. A major difficulty in the computational prediction of low Reynolds number aerodynamic flows is the fact that the flow has a tendency to separate under relatively mild adverse pressure gradients. In addition, the possibility of isolated separation bubbles and laminar-turbulent transition can also cause significant turbulence modeling issues.

Further, unlike in fixed wing vehicles or even rotary wing vehicles in forward flight, the flow-field of hovering rotors is significantly influenced by the trailed wake system since it remains in the proximity of the rotor at all times. Therefore, an accurate representation of the tip vortex formation and evolution is essential in achieving high fidelity performance predictions of hovering MAV. The desire to better understand tip vortex formation is evidenced by the large volume of computational, experimental and analytical studies performed over the past 30 years, [1–5]. However, the authors of this work have not found any validated computational studies of near-field low Reynolds number tip vortices. OVERTURNS, a RANS code, has been validated for a variety of high Reynolds number compressible flows involving fixed wing and rotor tip vortices, e.g. [6]. With the recent implementation of low Mach preconditioning into the OVERTURNS algorithm, the present work seeks to extend the validation of the code to low Reynolds number and low Mach tip vortex formation.

Methodology

The computations are performed using the overset structured mesh solver OVERTURNS [6]. This code solves the compressible RANS equations using a diagonal form of the implicit approximate factorization method developed by Pulliam and Chaussee [7]. In the present case, since low Mach numbers are involved, the preconditioning of Turkel [8] is implemented to improve convergence

and accuracy. The inviscid terms are computed using a third order MUSCL scheme utilizing Koren's limiter with Roe's flux difference splitting and the viscous terms are computed using second order central differencing.

The Spalart-Allmaras [9] turbulence model is employed for the RANS closure. This one-equation model has the advantages of ease of implementation, computational efficiency and numerical stability. The turbulence model equations are solved in an uncoupled manner with the NS equations. The implicit second order backward difference scheme is used with Newton sub-iterations for time integration. The implicit inversion is done using Diagonally Dominant ADI (DDADI) scheme. The convection terms are discretized using second order upwind scheme and the diffusion terms are discretized using second order central differences. The production term in this eddy-viscosity model is modified [6] to account for the reduction of turbulence in the vortex core due to flow rotation effects.

Infinite Span Validation

A significant issue concerning MAV wing and rotor design is the tendency for the flow to separate at lower angles of attack compared to higher Reynolds number applications. As a result, a number of researchers, [10, 11] have shown that for the Reynolds numbers typical of rotary MAV, thin cambered airfoils offer superior stall characteristics and aerodynamic performance. Mueller [10] has conducted extensive experimental studies on airfoils of this type at Reynolds numbers ranging from 60,000 to 200,000. Mueller's wing had a semi-span aspect ratio of 3.0 and used a circular arc airfoil with 5% camber and 1.93% thickness, see Fig. 1. Figure 2 shows a 2D computational validation of some of the results from Mueller's work at $Re = 60,000$ and $M = 0.016$. Computations are performed on a mesh of size 267×85 points in the streamwise and the normal direction respectively.

The lift predictions [12] are quite good with slightly lower predictions for C_{Lmax} and stall angle. Drag estimates show substantial under-predictions at lower angles of attack and slight over-predictions at higher angles. This is most likely caused by erroneous prediction of flow separation characteristics resulting from the turbulence model's difficulty in predicting transitional behaviors. In a similar validation of the present algorithm, Schroeder [13] notes that at lower angles of attack, the fully turbulent assumption of the present implementation of the Spalart-Allmaras model may underestimate the length of the laminar separation bubble, resulting in more attached flow and a lower drag. At higher angles of attack, the fully turbulent assumption may over-predict the levels of turbulence, resulting in increased separation

and higher drag. It should also be noted that Mueller's airfoil is prone to separation on the lower surface at low angles of attack, thus the correct calculation of this behavior makes accurate predictions of force for angles of attack near 0° more challenging. Nevertheless, this study serves as a demonstration of the capabilities of the low Mach preconditioner and turbulence model to deliver acceptable performance predictions under typical MAV operating conditions.

It has been recognized that wind tunnel data for flows involving separation cannot be assumed to be completely two dimensional because of the interaction with the side walls [14]. Schroeder [13] has demonstrated better validation of drag data for 3D wings in the wind tunnel set-up of Mueller [10]. Thus, these reasonably accurate infinite span performance predictions justify moving towards finite wing studies where the focus is not on performance, but on accurately predicting the flow field associated with the formation and evolution of the tip vortex.

Fixed-Wing Validation

The numerical algorithm is validated in the finite-span case using measurements made by Zuhai [5] on a NACA 0012 wing of aspect ratio 4.61 with a rectangular tip. Vortex velocity profiles were obtained using 2 and 3-component PIV techniques at $x = 1, 2, 3$ and 4 chords downstream of the trailing edge. Experiments were conducted at a Reynolds number of 9040, Mach number of 0.004 and at angles of attack ranging from $\alpha = 0^\circ$ through 10° . For these lower Reynolds numbers, the viscous forces become significant and Batchelor's analysis [4] shows that the viscous head loss term can overpower the inviscid acceleration mechanism and lead to an axial velocity deficit. In the present validation, the Zuhai experimental data shows the expected core axial velocity deficit in all cases. Computations are performed on a mesh of $369 \times 121 \times 111$ streamwise, spanwise and normal points, respectively (Fig. 3). To help ensure an accurate and stable simulation, OVERTURNS was run at a Mach of 0.05 rather than the lower experimental value. Since the Mach numbers involved in these studies are well within the incompressible limit, it is expected that small variations in Mach number will not have a significant effect on the final results.

As mentioned previously, because of the increased tendency for flow separation, MAV usually employ thin airfoil sections. Thus as we might expect with the relatively thick NACA 0012, regions of flow separation exist along much of the span, especially at low angles of attack. Spanwise shedding interacts with the developing tip vortex causing it to deform, resulting in some of the oscillations in the velocity profiles shown in Fig. 4. At high

angles of attack, the strength of the tip vortex is sufficient to generally outweigh the effect of these interactions. However, at angles of attack near 4° and below, the computed strength of the forming vortex is of the same order of magnitude as the spanwise shed vorticity. This causes a significant delay in the formation of a coherent vortex to streamwise location of up to 3 chords downstream. Because the experimental profiles are obtained by an ensemble average of instantaneous velocities, closer to the wing, these unsteady interactions are probably not accurately represented. For the purposes of validation, only the instantaneous profiles of the relatively steady tip vortex at angles of attack greater than 4 degrees are presented here.

The computed axial and swirl velocity profiles [12] in the tip vortex at $x/c = 1$ and 4 are given for $\alpha = 6, 8$ and 10 degrees in Fig. 4. In general, the computed axial velocity profiles show good agreement with the experiment aside from a tendency to slightly over-predict the magnitude of the axial velocity deficit. There is also an over-prediction of the effect of a secondary structure as can be seen on the inboard side ($r/c < 0$) of the axial velocity profiles at the $x/c = 1$ stations. Although especially pronounced for the 8 and 10 degree cases, these disturbances weaken by $x/c = 4$ producing smooth profiles between $r/c = -0.1$ to $r/c = -0.2$ for all angles of attack.

Note the relatively large core radius sizes resulting from the low Reynolds number. A typical core radius for a moderate Reynolds number of 200,000 may be on the order of $0.04c$ [15]. As seen in Fig. 4, the core radius is significantly larger ($r \approx 0.1c$) at the $x/c = 1$ station. The core radius and peak swirl velocities are notably under-predicted at 6 degrees, however the core radius is captured well at 8 degrees and both the swirl and radius size are in good agreement with the experiment at 10 degrees. The under-predictions may result from under resolving the vortex formation region at the blade tip. Although the magnitude of the swirl velocities is under-predicted outside of the core flow region, it is worth noting that the velocity gradients in this zone are predicted quite well in all cases. Again, the trend of improving results with increasing angle of attack may be attributed to the increasing margin between the strength of the tip vortex and the strength of the spanwise shedding. For rotors, the problems encountered with spanwise shedding in the fixed-wing case can be expected to be exacerbated by the direct influence of tip vortices trailed from the previous blade.

Hovering Rotor Validation

With validation of the predictive capability of OVERTURNS for low Mach number and Reynolds numbers in

2D and 3D fixed wing, the extension is made to the rotor case by exploring the experimental results obtained by Hein and Chopra [16] and Ramasamy et al. [17] on hovering rotors. The first case is used to demonstrate the capability of OVERTURNS to predict the overall performance, while the second case will be used for a more complete validation which include performance and flow field predicting capability.

Micro-rotor 1 (Hein and Chopra)

The experimental setup consists of a two-bladed rotor operating at a tip Mach number of 0.114 and tip Reynolds number of 51,200. The untwisted rectangular blades had an aspect ratio of 3.81 and used a 7% curvature circular arc airfoil with a thickness of 2.75%, qualitatively similar to the Mueller airfoil studied in the 2D validations. Performance data were obtained at collective angles of $\theta_o = 4, 6, 8, 10, 12$ and 14 degrees. A two mesh overset system with a body conforming blade mesh and a cylindrical background mesh was used. The blade mesh has $267 \times 185 \times 99$ points in the streamwise, spanwise and normal directions respectively and the background cylindrical mesh has $127 \times 186 \times 198$ points in the azimuthal, radial and vertical directions respectively, Fig. 5. Hole-cutting technique is used to blank out the portion of the background mesh that overlaps with the blade mesh. Information is exchanged from one grid to the other by means of interpolation. Certain geometric modifications are made to ensure high mesh quality. As opposed to the actual blade, the modeled leading edge and the tip are rounded, and the trailing edge comes to a sharp point.

Performance Comparison

Figure 6 shows the convergence of the thrust coefficient [12] for a sample set of collective angles. It can be seen that it is fairly converged for all the angles shown.

Figure 7 compares the performance results with those obtained in Hein and Chopra's experiment. Notice that the thrust coefficient, which is primarily a function of inflow, is predicted well. The figure of merit (FM) and C_P however, which are strongly related to the drag (and thus the amount of separation), show poor comparisons. The source of these discrepancies is most likely three-fold. One cause is the inability of the turbulence model to predict transitional behaviors as discussed during the infinite span validation. Secondly, the large boundary layer thickness and susceptibility of the flow to separation for low Reynolds numbers suggests that the aforementioned geometric differences in the modeled and experimental rotor may cause significant variations in parameters that are sensitive to these effects. The value of $C_{d0} = 0.068$ and $k = 1.2$ were determined by curve fitting the experi-

mental results. Then $k = 1.2$ was held constant to curve fit the computational results. For idealized momentum theory, k is 1 and C_{d0} is 0. The power predictions are shown along with the simple momentum theory power predictions for both experimental and computational data in Fig. 7 (d). It can be seen that the discrepancy in C_{d0} of approximately 50% represents a major contribution to the under-prediction of the power. Finally, the computations did not model the influence of the experimental rotor mounting apparatus. In flow visualizations taken from [16], the mounting clearly introduces an obstacle near the blade root which may result in increased power estimates.

The present calculations are in the rotor blade frame where source terms are added to the momentum equation to allow for the rotation (there is zero grid velocity in the rotor blade frame). The flow relative to the rotor blade should become stationary in time. The alternative is to calculate things in the inertial system where the blade motion is accounted for by the grid velocities. In this system the flow is unsteady as the blade rotates. This would require a time-accurate preconditioner which allows for time accuracy of the unsteady calculations. In a separate study of a non-preconditioned regular size rotor case, the authors have noticed some discrepancy in the power predictions between blade frame and inertial frame calculations. Details of this will be looked into as a part of the future work.

Circulation

The bound circulation Γ_b over the rotor span for each collective angle is plotted in Fig. 8. There is the expected monotonic increase moving from the root towards the tip which leads into a zone of unsteady variations beginning at approximately 80% span. Continuing towards the tip, the variations persist until the local effect of the forming tip vortex is indicated by a large spike in circulation. The variations in Γ_b near the tip region are partially caused by interactions with the vortices from the previous blade and previous rotor revolutions. Another source of these oscillations could be the unsteady trailed wake structures as seen from Fig. 10. This notion is supported by the increase in the extent and amplitude of variations with decreasing collective angle, since lower induced velocities in the wake give rise to vortices that linger near the rotor plane for longer periods of time. Additionally, the unsteady shear layer convecting off the trailing edge can contribute to fluctuation. Another cause of the variations in Γ_b is the trailing edge shear layer. In higher Reynolds number cases this unsteady flow region is typically smaller than the grid can accurately capture. However, the shear layer in the present case is thick enough to be at least coarsely resolved and have its unsteady in-

fluence felt at the blade. This is similar to the difficulties encountered at low angles of attack in the fixed wing case discussed previously. These two factors result in an indefinite value of the peak bound circulation. At $\theta_o = 4^\circ$, these effects result in the strength of the tip vortex circulation peak at $y/R = 1$ being less than the peaks in circulation just inboard of the tip.

Another effect of lower collective angles is the tighter grouping of vortices in the wake. As a result, computing vortex circulation by integrating a circuit around a single vortex (as is done in this study) may yield misleading results since the choice of circuits will include effects from neighboring vortices. This problem manifests at $\theta_o = 4^\circ$ in the fluctuating prediction of vortex circulation shown in Fig. 9. Other collective angles essentially show a constant circulation strength with wake age, which agrees with Helmholtz's 3rd vortex theorem which requires a conservation of circulation. This result is also a testament to the sufficient spatial resolution of the vortex in the far-field.

Comparing the bound and vortex circulations, we find that for each collective angle, $\Gamma_v \approx \Gamma_b$. These results, listed in Table 1, are most likely overestimated because of the ambiguity in measuring the bound circulation near the tip mentioned earlier. Nevertheless, within the margins of this ambiguity, the percentage of circulation entrained into the tip vortex is markedly greater than is typically reported in higher Reynolds number studies. As an example, Bhagwat and Leishman [21] report $\Gamma_v/\Gamma_b \approx 50 - 70\%$ for a larger aspect ratio blade at $Re = 2.7 \times 10^5$. From Fig. 9, the vortex appears to be fully rolled up by the wake age of $20^\circ - 40^\circ$. This is an expected result for an untwisted rotor blade.

Vortex evolution

Figure 11 shows the computed tip vortex core radius and peak swirl velocities over one rotor revolution. The asymmetry of the swirl velocity profiles result primarily from the influence of the rotor slipstream on the portion of the tip vortex that is inboard of the wake boundary. Note that just after the vortex passes under the second blade at $\theta_o = 180^\circ$, the inboard portion of the vortex is accelerated while the outboard swirl velocity decay continues relatively unaffected. This is accompanied by a sudden decrease in the core radius.

Micro-rotor 2 (Ramasamy et al.)

The experimental setup consists of a two-bladed rotor operating at a tip Mach number of 0.085 and tip Reynolds number of 36,450. The untwisted rectangular blades had an aspect ratio of 4.39 and used a 3.3% curvature circular arc airfoil with a thickness of 3.7%. High reso-

lution flow visualization and particle image velocimetry (PIV) flow-field data and performance data is available at various collective angles. Computation is performed for the case with collective angle of 12° . A two mesh overset system with a body conforming blade mesh and a cylindrical background mesh was used. The blade mesh has $267 \times 185 \times 99$ points in the streamwise, spanwise and normal directions respectively and the background cylindrical mesh has $127 \times 186 \times 198$ points in the azimuthal, radial and vertical directions respectively. Similar to Micro-rotor 1, certain geometric modifications are made to ensure high mesh quality. As opposed to the actual blade, the modeled leading edge and the tip are rounded, and the trailing edge comes to a sharp point.

Flow-field Visualizations

Figure 12 shows iso-surfaces of the vorticity magnitude near the blade surface. It is evident that the tip vortex flow-field is extremely complicated because of the presence of a variety of secondary structures near the blade tip. The origin of these structures can be discerned from Fig. 13. While initial traces of the tip vortex can be seen slightly upstream of the quarter-chord point, secondary vortices originate from the leading edge as well as from the separation of the cross-flow boundary layer rolling over the rounded tip. Within a short distance downstream of the trailing edge, these structures appear to have merged with the tip vortex (as seen from the coherent iso-surface in Fig. 12). In addition to the secondary vortices, a large number of additional vortical structures are found near the trailing edge of the blade over most of the span. These structures are formed as a result of flow separation near the blade trailing edge and are seen to persist over large wake ages.

As mentioned in the previous paragraph, a number of vortical structures mask the flow-field of the tip vortex. In order to extract only the rotational flow regions and not the highly strained regions, the so-called q -criterion [18] is shown in Fig. 14. The resolution of the tip vortex until 3 blade passages is clearly evident. Beyond this wake-age, the background mesh becomes too coarse to accurately represent the details of the tip vortex. An interesting feature revealed from this figure is the fact that while the tip vortex is smooth initially, it seems to get twisted near the first blade passage. This is because of the fact that it is embedded in a highly strained field due to the presence of the evolving tip vortex (note that the vertical convection of the tip vortex is relatively low before the first /pass as has been well documented [19, 20]) and other near-blade structures. It is also seen that after the first pass, the vortex becomes wavy along its axis, thus suggesting an instability.

Further evidence of the interaction between differ-

ent turns of the tip vortex can be seen in Fig. 15, in which, vorticity magnitude contours are shown along an azimuthal plane of the background mesh. The tip vortex, after its first blade passage is seen to interact with the in-board wake as well as the second blade passage, both of which introduce a strain-field.

Performance Comparison

Experiments were performed on different variations of the baseline airfoil cross-section (blunt at both leading and trailing edge). The cross-section with sharpened leading and trailing edge (SLT) resembles closely to the one used for computations, with the difference of a slightly rounded leading edge for the modeled geometry. Table 2 shows the performance comparison with the baseline and SLT data. As expected, the thrust is predicted well, with the values closer to the SLT case. Surprisingly, even the power prediction is good, the value lies between the baseline and the SLT cases. It should be noted that the experimental results were obtained by removing the contribution from tares (obtained from tests without the blades attached to the hub). However, the contribution from tares were only about 1% of the total value and therefore insignificant. An interesting thing to notice is that a slight variation in the experimental geometry caused significant difference in the performance data, especially the figure of merit. This points to the importance of accurately modeling the geometry, also suggesting that the difference between the modeled and the actual geometry could be the main reason for the discrepancies in the power prediction of the Micro-rotor 1.

Flow-field Comparison

Figures 16 and 17 compares the computed swirl velocity contours with the experimental results at the azimuth locations, 30° and 60° , respectively. The contours shows good agreement except a slight over-prediction in the core radius of the tip vortex. The experiments also show a more turbulent flow-field compared to the computations. Figures 18 and 19 show the comparison of streamwise vorticity contour at the azimuth locations, 30° and 60° , respectively. The agreement is very good with reasonably accurate prediction of the amount of wake contraction. Again we see a slight over-prediction in the tip vortex core radius. The reason for this could be due to the under-resolution of the tip vortex formation resulting in excessive numerical dissipation which leads to a non-physical growth of the core radius.

Vortex Structure comparison

Figure 20 shows the comparison of swirl velocity profile at the wake ages of 30° , 60° , 210° and 240° . At

all azimuth locations, the core radius is over-predicted. However, the rate of core growth is predicted accurately, see Fig. 22(a). This supports the fact that the tip vortex formation is under-resolved, while its evolution is well resolved. Therefore, an unphysical growth in the core radius is observed initially, there after, the core grows in the correct manner. Similar to core radius, the peak swirl velocity is over-predicted at all wake ages, while its decay rate is predicted accurately, see Fig. 22(b). The main reason for this is due to an over-prediction in the amount of vorticity entraining into the tip vortex, clearly seen in Fig. 23, which will lead to a larger swirl velocity. The inadequacy of the Spalart-Allmaras turbulence model in a non-isotropic environment such as those found near the regions of tip vortex formation could be the major cause for this discrepancy. The above notion is supported by the streamwise vorticity profile plot, Fig. 21. The plot shows a trend of improving prediction with the wake age. The peak vorticity is under-predicted at smaller wake ages and slightly over-predicted at larger wake ages. However, the area under the curve shows an increased vorticity prediction at all azimuth locations.

Conclusions

A computational validation of a compressible RANS code was performed for the model cases of a 2D airfoil, a fixed-wing and a hovering rotor, each operating at the low Reynolds and Mach numbers typically associated with MAV.

2D airfoil : Lift predictions of the experimental data in the 2D case were good, however drag is under-predicted, especially at low angles of attack. This may be due to the difficulty in accurately predicting transition as well as experimental uncertainty.

3D Fixed wing : With respect to the strength of the tip vortex, strong unsteady shedding resulting from the thick NACA 0012 airfoil section was observed along most of the span in the fixed-wing validation. At angles of attack greater than 4° , the computed tip vortex was strong enough to remain relatively steady at both the $x/c = 1$ and 4 stations. The comparisons of these results with experiment showed good capture of the axial velocity deficit, peak swirl velocity and core radius size at $\alpha = 10^\circ$, although the accuracy of these predictions degraded as α decreased.

Hovering rotor : The tip vortex formed on MAV rotor blades was observed to interact with secondary vortices early in its development along the chord. Interactions with other secondary vortical structures formed from unsteady shedding at the blades trailing edge continued in the near and far wake. After the first passage of the tip vortex under the blade, the vortex experienced

some destabilization as it was influenced by the strain field from both the blade and the inboard wake sheet. The blade passage also resulted in an increased vertical convection rate and reduction in vortex core size. Performance predictions for Micro-rotor 1 were similar to the 2D case in that drag was under-predicted. However, the power prediction for Micro-rotor 2 was good. Some of this discrepancy could be attributed to the difference between the actual and the modeled geometry. The thrust coefficient, as it is mostly an inviscid mechanism was captured quite well.

Vortex circulation was found to be nominally constant over at least the first 180° of wake age, a significant result indicative of a spatially well resolved vortex. Calculations also show that the magnitude of vortex circulation was almost equal to the peak bound circulation. It was noted however that the difficulties in discerning the peak bound circulation likely caused this to be an overestimate. Also, the inadequacy of the turbulence model could have caused an over-prediction in the tip vortex circulation.

Prediction of the vortex structure was found to be reasonable with the exception of initial wake ages. The discrepancy could arise due to under-resolved tip vortex formation leading to an unphysical initial core growth. However, the vortex core evolution resembles the experimental result. It was surmised that the over-prediction in the swirl velocity could have resulted from the over-prediction in the vorticity of the tip vortex.

The results of this work demonstrate the applicability of RANS solution techniques to the operating conditions typical of hovering MAV. The ability of OVERTURNS to quantitatively reproduce experimental results and provide insight into localized flow phenomena serves as a strong incentive to continue computational MAV study with similar algorithms. While inviscid effects seem to be satisfactorily represented, drag prediction seems to be more sensitive to the details of the leading edge and trailing edge geometries and hence a more difficult problem.

Future Work

The results of this investigation illustrate the significance of both accurately modeling the experimental geometry and sufficiently resolving the regions of tip vortex formation. In continuing this work the authors plan to develop a more accurate computational representation of the sharpened leading and trailing edges of Micro-rotor 1 blade and the Mueller airfoil. It is hoped that these improvements will yield better predictions of the separation locations and thus better predictions of C_{d0} and other performance parameters that are tied to viscous mechanisms.

The unsteady nature of the flow-field, especially near the blade was clearly seen. However, all the computations

were performed in a non-time accurate mode due to the limitation of the current preconditioner in OVERTURNS. As a continuing work, a modified preconditioner will be implemented, which will allow time accurate computations for these low Mach number cases. This will also enable computations in the inertial frame instead of the blade frame, which might further improve the predictions.

Improved prediction of vortex structure at the initial wake ages will be attained by increasing the grid resolution near the tip of the blade, leading to a more accurate representation of the tip vortex formation. Moreover, computations performed using higher order scheme could reduce some of the numerical dissipation. The use of fifth order scheme for the inviscid terms and fourth order scheme for the viscous terms will be considered. The resolution requirements at the Reynolds numbers in this study are small enough that a Large Eddy Simulation (LES) is under consideration for future investigations. This may be pursued initially by implementing a hybrid RANS/LES simulation in an effort to efficiently calculate attached flow regions while maintaining accuracy in separated flow.

Acknowledgments

This work is sponsored by the Army Research Office Contract MURI ARMY-W911NF0410176. Opinions, interpretations, conclusions, and recommendations are those of the authors and are not necessarily endorsed by the United States Government. The authors would like to thank the Technical Monitor Dr. Tom Doligalski and the MURI review team for their encouragement and support. The authors are also greatly appreciative of Eric Schroeder's initial work in validating the Mueller and Micro-rotor 1 results.

References

- [1] Moore, D.W. and Saffman, P.G., "Axial flow in laminar trailing vortices," *Proc. R. Soc. Lond. A.*, Vol 333, pp. 491–508.
- [2] Chow, J. S., Killiac, G. G. and Bradshaw, P., "Mean and Turbulence Measurements in the Near Field of a Wingtip Vortex," *AIAA Journal*, Vol. 35, No. 10, 1997.
- [3] Devenport, W. J. Rife, M. C., Liapis, S. I. and Follin, G. J., "The Structure and Development of a Wing-tip Vortex," *Journal of Fluid Mechanics*, Vol. 312, 1996.

- [4] Batchelor, G. K., "Axial Flow in Trailing Line Vortices," *Journal of Fluid Mechanics*, Vol. 20, 1964.
- [5] Zuhail, L. R., "Formation and Near-Field Dynamics of a Wing Tip Vortex," *PhD Thesis, California Institute of Technology*, 2001.
- [6] Duraisamy, K., "Studies in Tip Vortex Formation, Evolution and Control," *PhD Thesis, Department of Aerospace Engineering, University of Maryland at College Park*, 2005.
- [7] Pulliam, T. H. and Chaussee, D. S. "A diagonal Form of an Implicit Approximate Factorization Algorithm," *J. Comp. Phys.*, Vol. 39, 1981.
- [8] Turkel, E., "Preconditioning Techniques in Computational Fluid Dynamics," *Annual Review of Fluid Mechanics*, Vol. 31, 1999, pp. 385–416.
- [9] Spalart, P. R. and Allmaras, S. R., "A One Equation Turbulence Model for Aerodynamics Flow," *AIAA Paper 92-0439*, 1992, pp. 1–22.
- [10] Mueller, T. J., "Aerodynamic Measurements at Low Reynolds Numbers for Fixed Wing Micro-Air Vehicles," Presented at the RTO AVT/VKI Special course on Development and Operation of UAV's for Military and Civil Applications, September 13–17, VKI, Belgium, 1999.
- [11] Laitone, E. V., "Aerodynamic Lift at Reynolds Numbers below 7×10^4 ," *AIAA Journal*, Vol. 34, No. 9, 1996.
- [12] Lakshminarayan, V.K., Bush, B.L., Duraisamy, K. and Baeder, J., "Computational Investigation of Micro Hovering Rotor Aerodynamics," *24th AIAA Applied Aerodynamics Conference*, San Francisco, California, June 5–8, 2006.
- [13] Schroeder, E., "Low Reynolds Number Flow Validation using Computational Fluid Dynamics with Applications to Micro Air Vehicles," *Master's Thesis, Department of Aerospace Engineering, University of Maryland at College Park*, 2005.
- [14] Spalart, P.R., "Trends in Turbulence Treatments," *AIAA Paper 00-2306*, 2000.
- [15] Heyes, A. L., Jones, R. F. and Smith, D. A. R., "Wandering of Wing-tip Vortices," *Proceedings of 12th International Symposium on Application of Laser Techniques to Fluid Mechanics*, 2004.
- [16] Hein, B. R. and Chopra, I., "Hover Performance of a Micro Air Vehicle: Rotors at Low Reynolds Number," *Proceedings of the American Helicopter Society International Specialists' Meeting on Unmanned Rotorcraft*, 2005.
- [17] Ramasamy, M., Johnson, B., and Leishman, J. G., "Toward Understanding the Aerodynamic Efficiency of a Hovering Micro-Rotor," *Proceedings of the American Helicopter Society International Specialists' Meeting on Unmanned Rotorcraft*, 2007.
- [18] Jeong, J. and Hussain, F., "On the Identification of a Vortex," *J. Fluid. Mech.*, 285, 1995, pp. 69–94.
- [19] Leishman, J. G., "Principles of Helicopter Aerodynamics," Cambridge University Press, 2002.
- [20] Duraisamy, K., Sitaraman, J. and Baeder, J., "High Resolution Wake Capturing Methodology for Accurate Simulation of Rotor Aerodynamics," *61st Annual Forum of the American Helicopter Society*, 2005.
- [21] Bhagwat, M.J. and Leishman, J.G., "Measurements of Bound and Wake Circulation on a Helicopter Rotor," *Journal of Aircraft*, Vol. 37, No. 2, 2000.

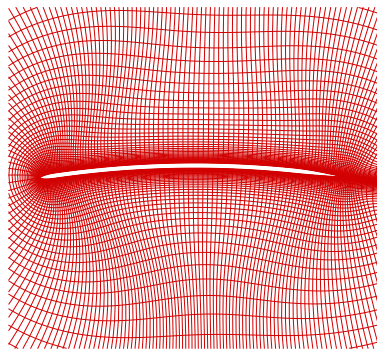


Figure 1: Mueller airfoil mesh.

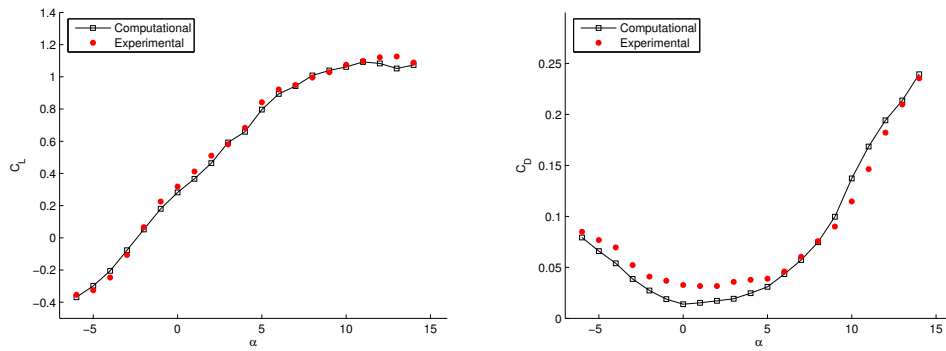


Figure 2: 2D validation with Mueller C_L and C_D experiment. $Re = 60,000$.

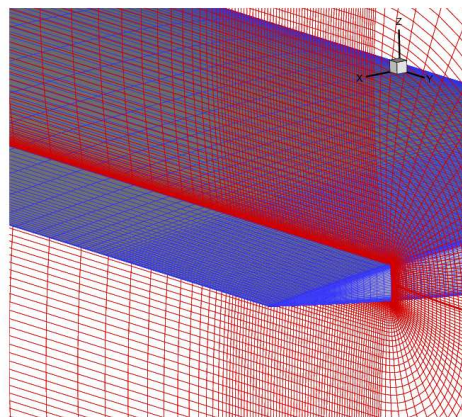
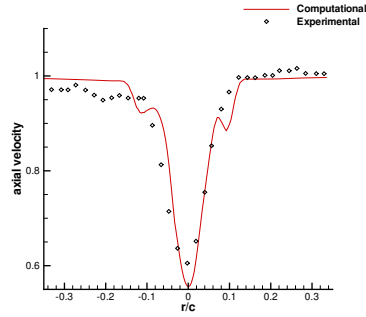
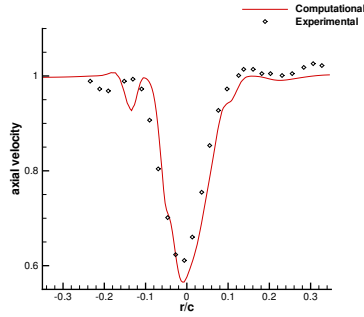


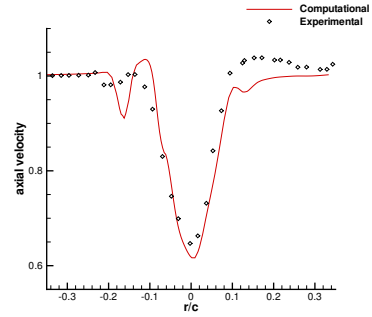
Figure 3: Computational mesh used for validation with Zuhai experiments.



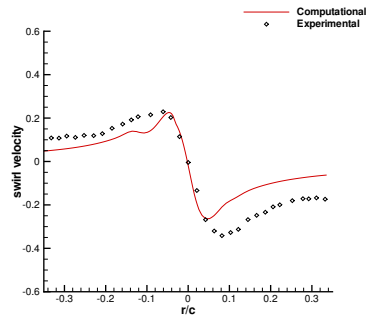
(a) $\alpha = 6^\circ, x/c = 1$



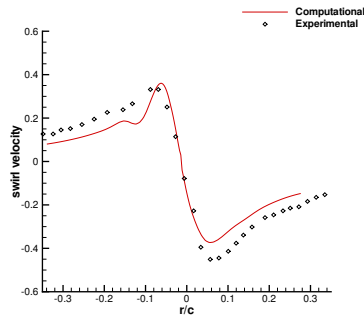
(b) $\alpha = 8^\circ, x/c = 1$



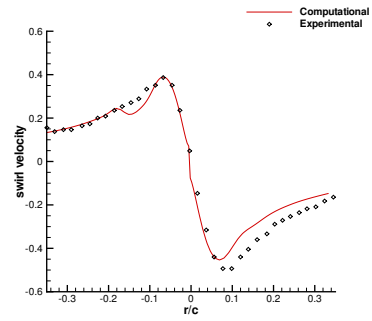
(c) $\alpha = 10^\circ, x/c = 1$



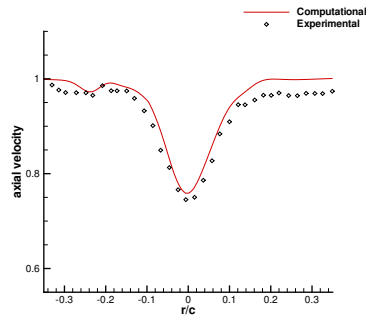
(d) $\alpha = 6^\circ, x/c = 1$



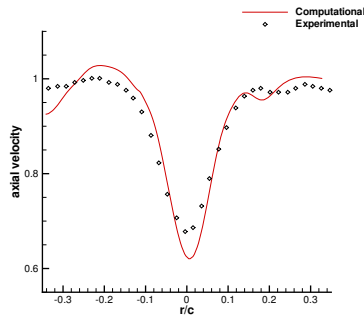
(e) $\alpha = 8^\circ, x/c = 1$



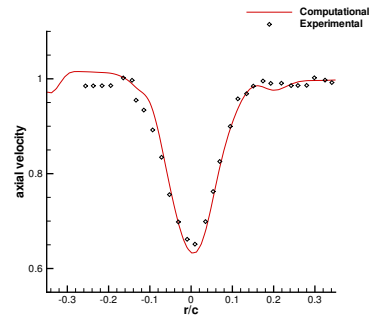
(f) $\alpha = 10^\circ, x/c = 1$



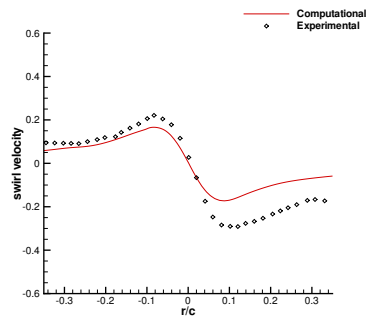
(g) $\alpha = 6^\circ, x/c = 4$



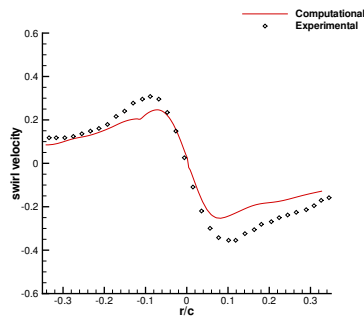
(h) $\alpha = 8^\circ, x/c = 4$



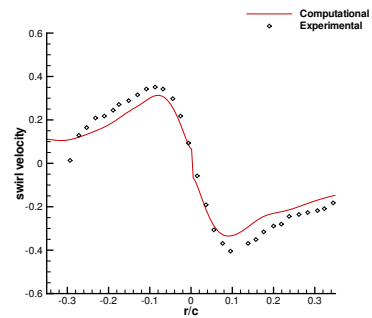
(i) $\alpha = 10^\circ, x/c = 4$



(j) $\alpha = 6^\circ, x/c = 4$



(k) $\alpha = 8^\circ, x/c = 4$



(l) $\alpha = 10^\circ, x/c = 4$

Figure 4: Swirl and axial velocity profiles for fixed wing, $Re = 9040$.

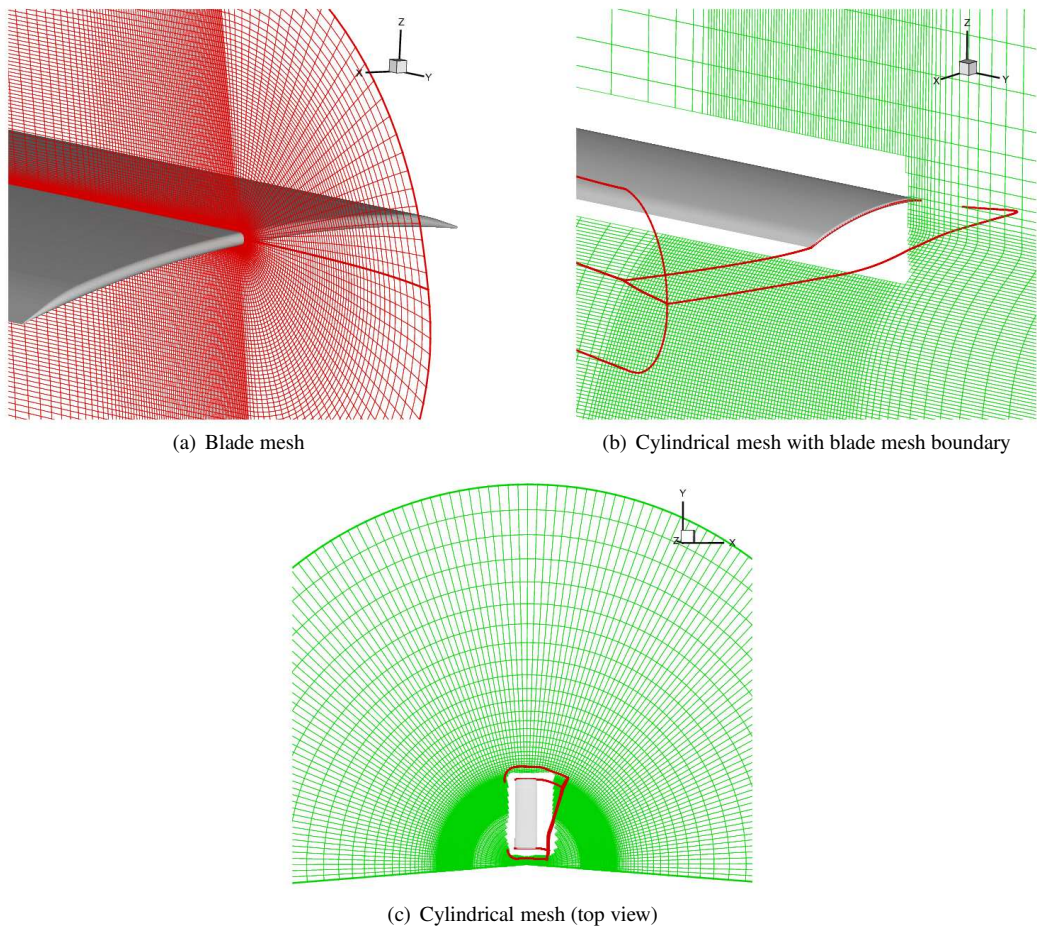


Figure 5: Computational mesh for Micro-rotor 1 comparisons.

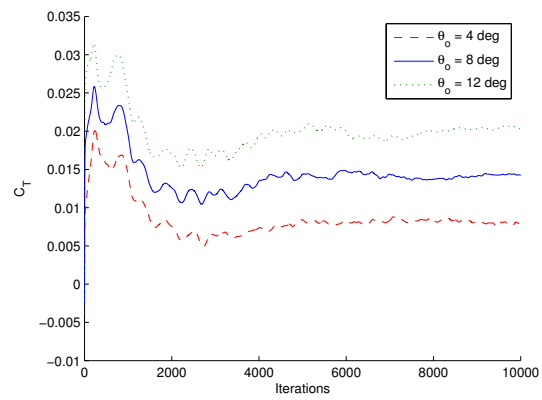
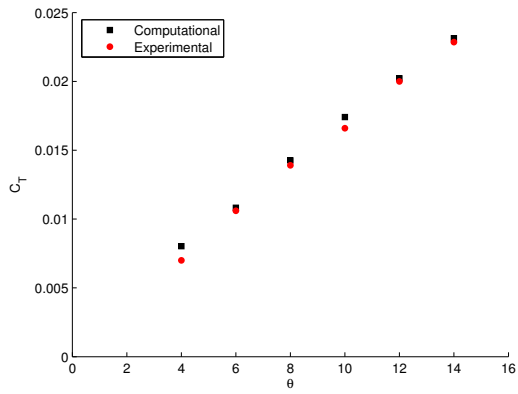
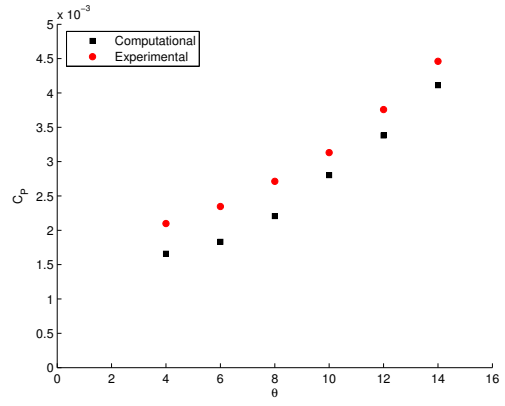


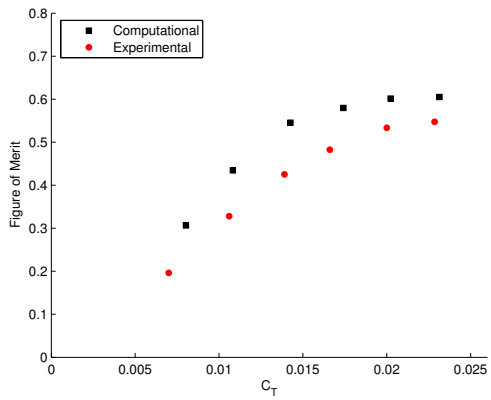
Figure 6: Plot showing the convergence of C_T for Micro-rotor 1.



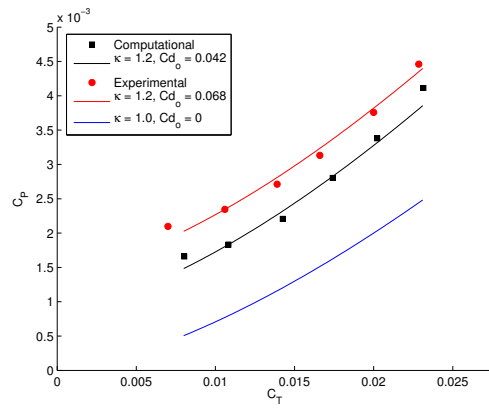
(a)



(b)



(c)



(d)

Figure 7: Computed and experimental performance for Micro-rotor 1.

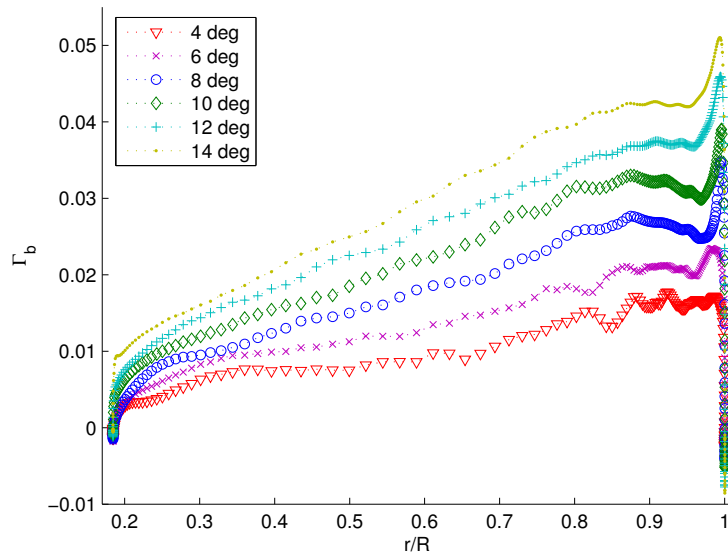


Figure 8: Non-dimensionalized bound circulation along rotor span for Micro-rotor 1.

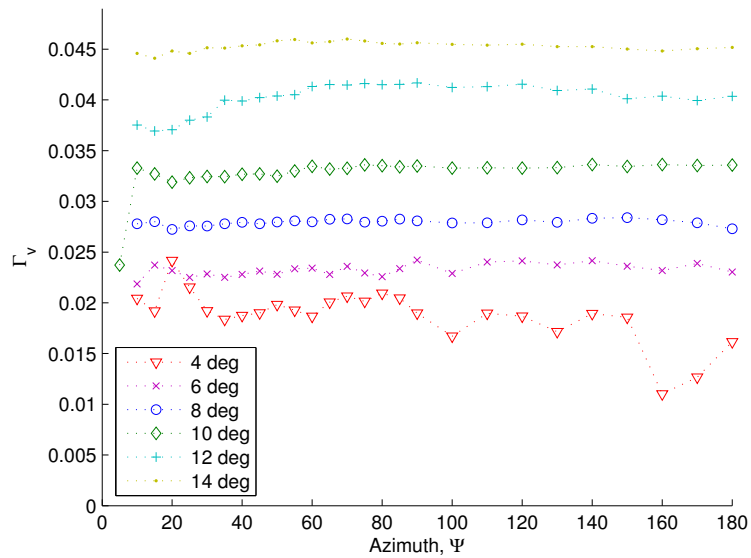


Figure 9: Non-dimensionalized vortex circulation as a function of wake age for Micro-rotor 1.

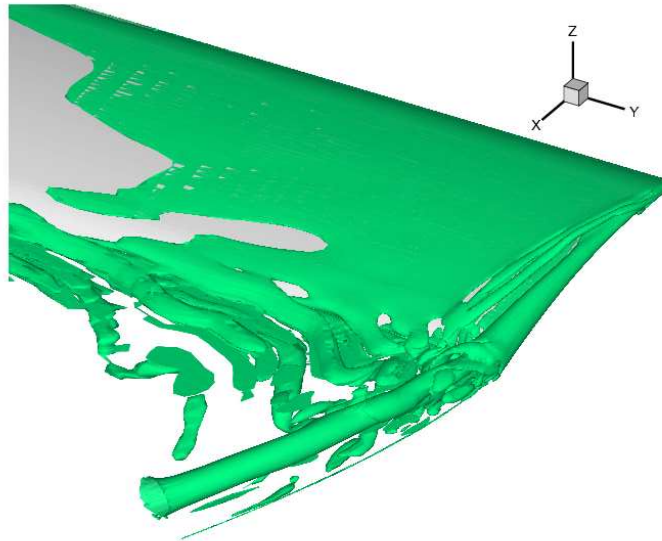


Figure 10: Iso-surfaces of vorticity magnitude $|\omega| = 5.0$ for hovering Micro-robot 1.

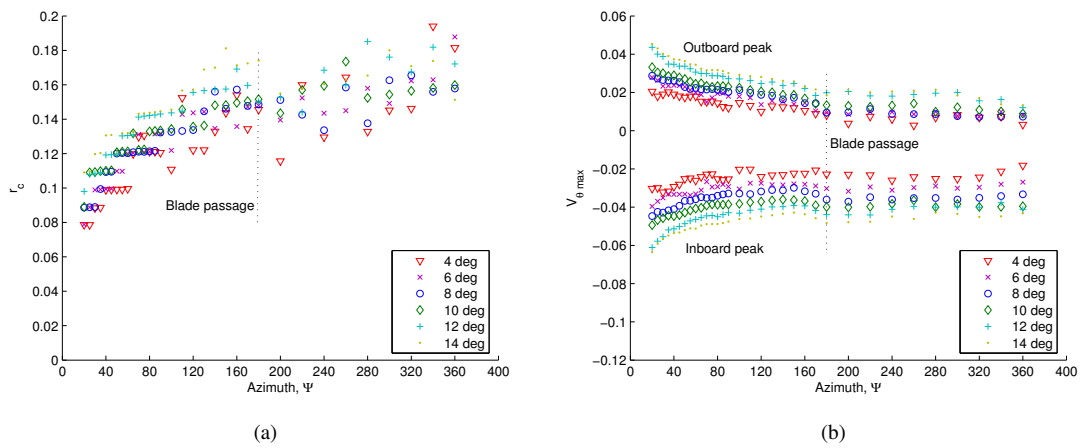


Figure 11: Tip vortex viscous core radius (a) and Peak tip vortex swirl velocity (b) with wake age, for Micro-robot 1.

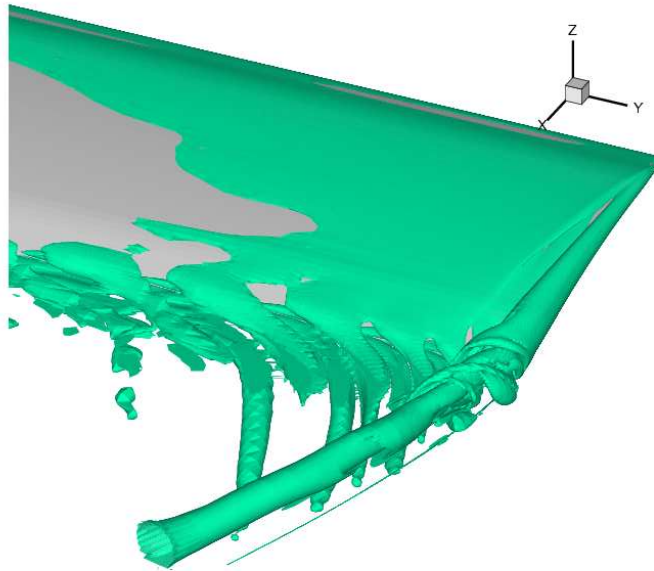


Figure 12: Iso-surfaces of vorticity magnitude $|\omega| = 5.0$ for hovering Micro-rotor 2.

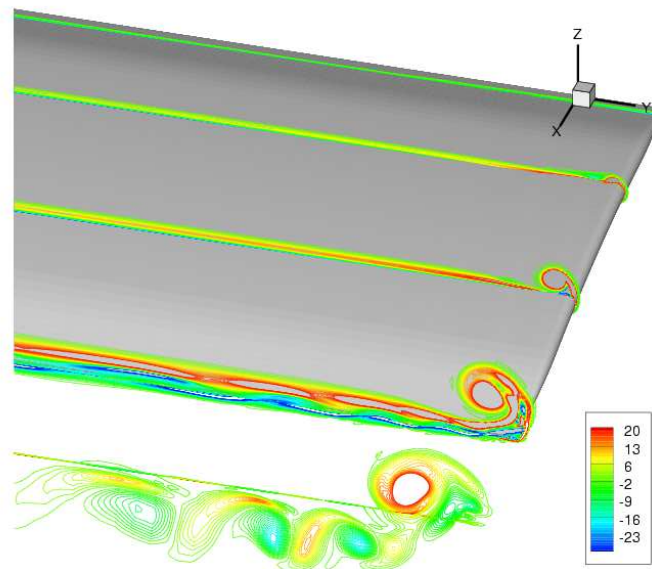


Figure 13: Contours of streamwise vorticity for Micro-rotor 2.

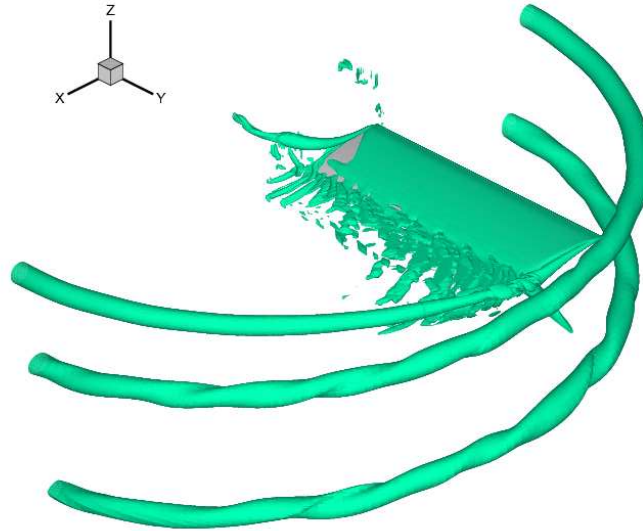


Figure 14: Iso-surfaces of second invariant of velocity magnitude $q = 1.0$ for Micro-rotor 2.

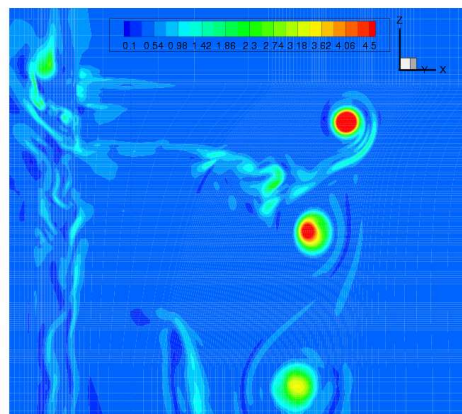


Figure 15: Contours of vorticity magnitude at $\psi = 60^\circ$ for Micro-rotor 2.

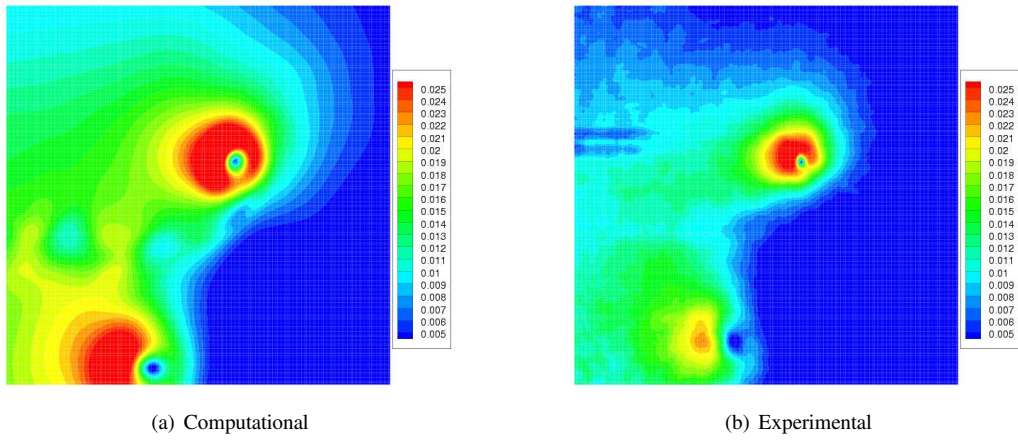


Figure 16: Swirl Velocity contours at $\psi = 30^\circ$ for Micro-rotor 2.

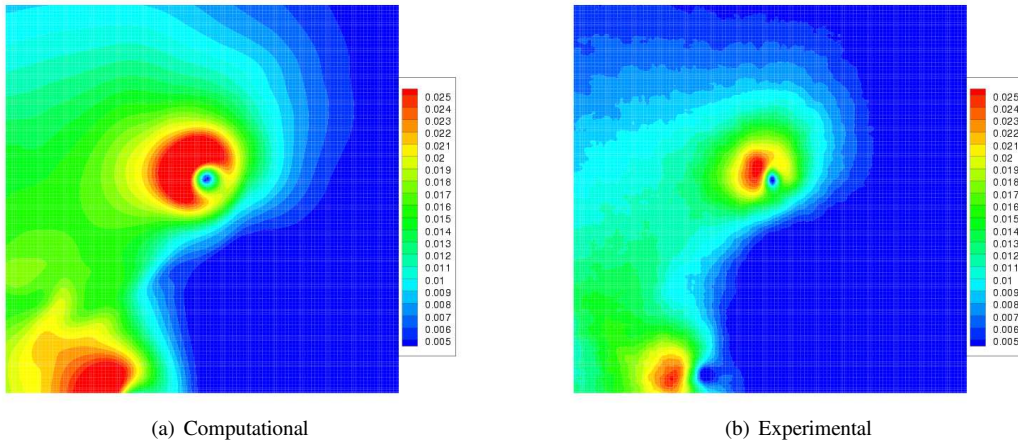


Figure 17: Swirl Velocity contours at $\psi = 60^\circ$ for Micro-rotor 2.

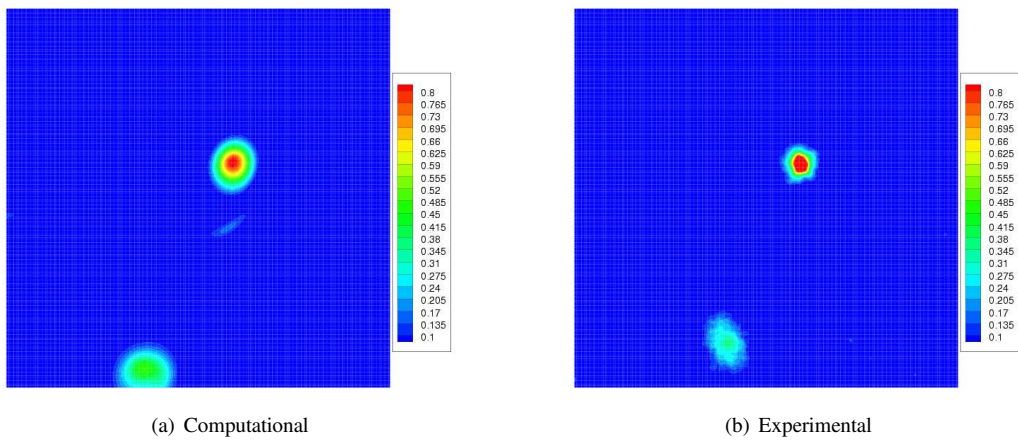


Figure 18: Streamwise Vorticity contours at $\psi = 30^\circ$ for Micro-rotor 2.

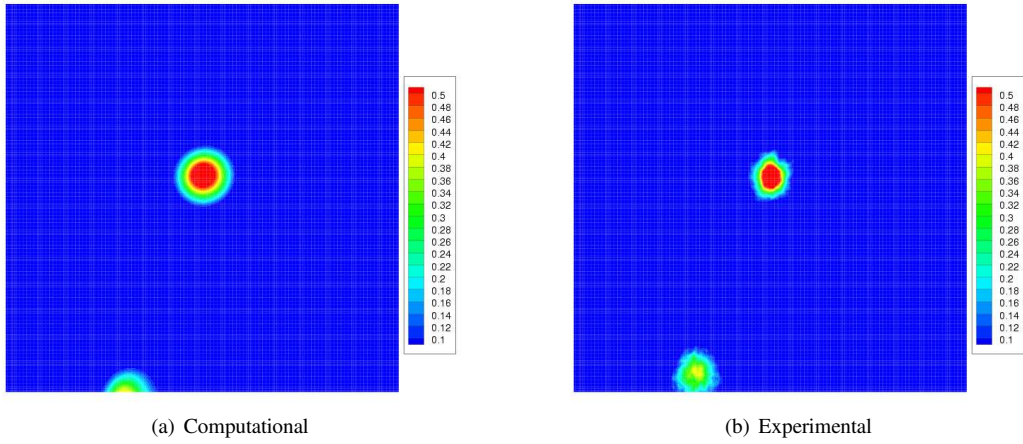


Figure 19: Streamwise Vorticity contours at $\psi = 60^\circ$ for Micro-rotor 2.

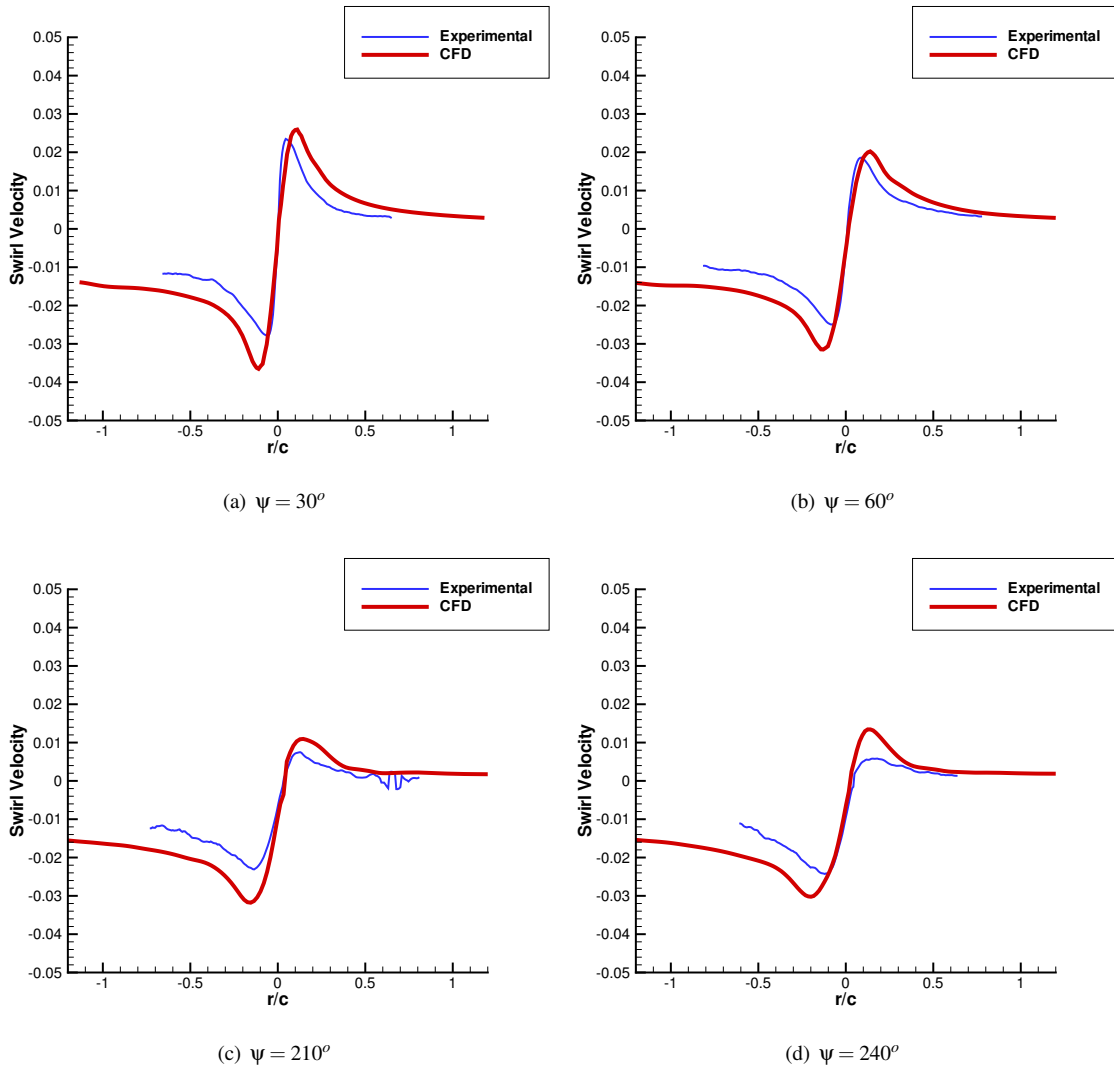
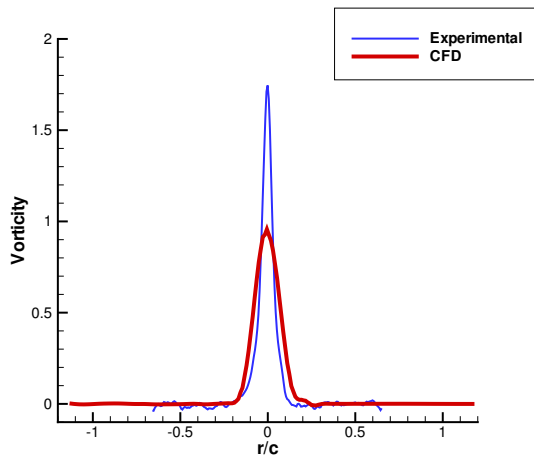
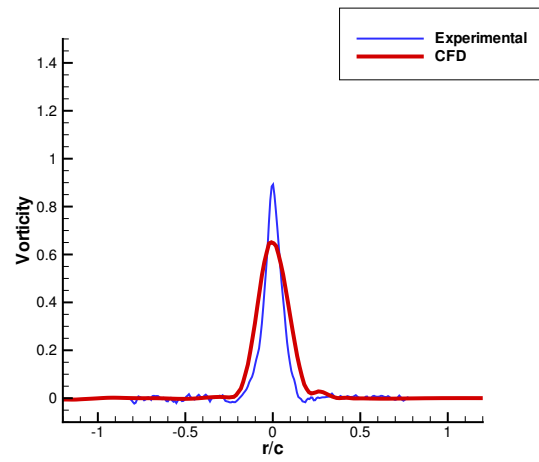


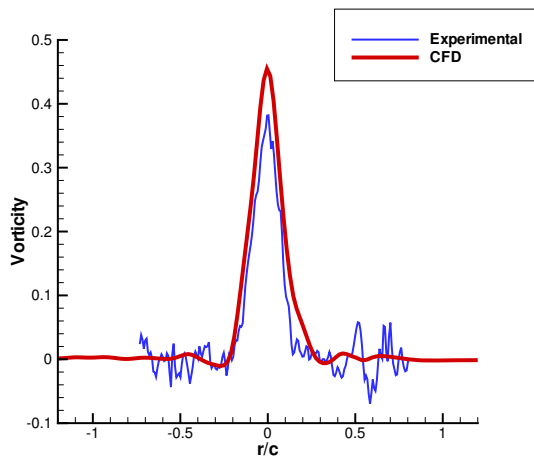
Figure 20: Swirl Velocity profile comparison for Micro-rotor 2.



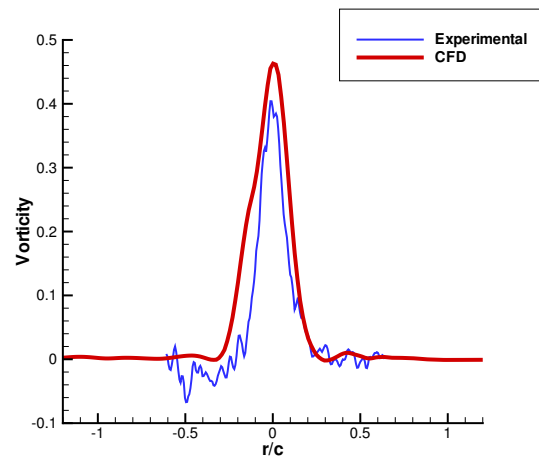
(a) $\psi = 30^\circ$



(b) $\psi = 60^\circ$



(c) $\psi = 210^\circ$



(d) $\psi = 240^\circ$

Figure 21: Streamwise vorticity profile comparison for Micro-rotor 2.

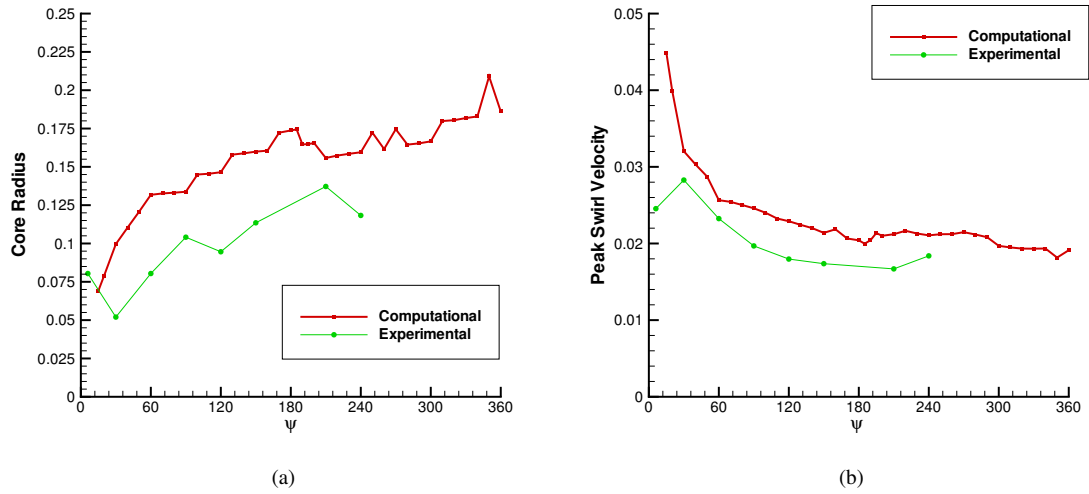


Figure 22: Tip vortex viscous core radius (a) and Peak tip vortex swirl velocity (b) with wake age, for Micro-rotor 2.

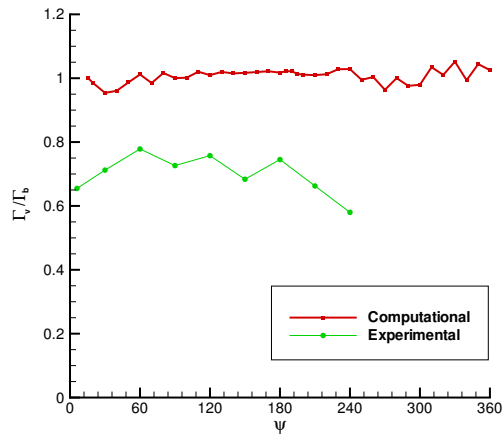


Figure 23: Ratio of vortex circulation to bound circulation with wake age for Micro-rotor 2.

θ_o	Γ_b	Γ_v	Γ_v/Γ_b
4	0.0177	0.0191	1.08
6	0.0212	0.0233	1.09
8	0.0277	0.0280	1.01
10	0.0330	0.0331	1.00
12	0.0374	0.0409	1.09
14	0.0427	0.0455	1.06

Table 1: Relationship between peak non-dimensionalized bound circulation and non-dimensionalized circulation in the tip vortex for Micro-rotor 1.

	C_T	C_P	FM
Computational	0.0169	0.00272	0.57
Expt. (baseline)	0.0159	0.00306	0.46
Expt. (SLT)	0.0172	0.00244	0.65

Table 2: Performance comparison for Micro-rotor 2.